



LAWRENCE  
LIVERMORE  
NATIONAL  
LABORATORY

# Effects of Boundary Conditions and Flow on the Kink Instability in a Cylindrical Plasma Column

I. Furno, T. P. Intrator, G. Lapenta, L. Dorf, D. D.  
Ryutov

February 8, 2007

Physics of Plasmas

## **Disclaimer**

---

This document was prepared as an account of work sponsored by an agency of the United States Government. Neither the United States Government nor the University of California nor any of their employees, makes any warranty, express or implied, or assumes any legal liability or responsibility for the accuracy, completeness, or usefulness of any information, apparatus, product, or process disclosed, or represents that its use would not infringe privately owned rights. Reference herein to any specific commercial product, process, or service by trade name, trademark, manufacturer, or otherwise, does not necessarily constitute or imply its endorsement, recommendation, or favoring by the United States Government or the University of California. The views and opinions of authors expressed herein do not necessarily state or reflect those of the United States Government or the University of California, and shall not be used for advertising or product endorsement purposes.

# Effects of boundary conditions and flow on the kink instability in a cylindrical plasma column

I. Furno<sup>1</sup>, T.P. Intrator<sup>1</sup>, G. Lapenta<sup>1</sup>, L. Dorf<sup>1</sup>, and D.D. Ryutov<sup>2</sup>

<sup>1</sup> *Los Alamos National Laboratory, M.S. E526, Los Alamos, NM 87545, USA*

<sup>2</sup> *Lawrence Livermore National Laboratory, Livermore CA 94551*

(Dated: September 26, 2006)

An experimental investigation of the kink instability is presented in a linear plasma column where one end is line-tied to the plasma source, and the other end is not line-tied and therefore free to slide over the surface of the end-plate. This latter boundary condition is a result of plasma sheath resistance that insulates, at least partially, the plasma from the end-plate. The helical  $m = 1$  kink mode is observed to grow when the plasma current exceeds a threshold and, close to the criticality, is characterized by an axial mode structure with maximum displacement at the free axial boundary. Azimuthal rotation of the mode is observed such that the helically kinked column always screws into the free axial boundary. The kink mode structure, rotation frequency and instability threshold are accurately reproduced by a recent kink theory [D. D. Ryutov, *et al.*, Phys. Plasmas **13**, 032105 (2006)], which includes axial plasma flow and one end of the plasma column that is free to move due to a perfect non-line-tying boundary condition which is experimentally verified. A brief review of the kink theory and its predictions for the boundary conditions relevant in the present experiments are presented.

PACS numbers: 52.35.Py, 52.30.Cv, 52.70.Ds, 52.70.Kz

## I. INTRODUCTION

The current driven kink instability is a magnetohydrodynamic (MHD) instability which affects current carrying plasmas in Nature and laboratory. Sakurai [1] was the first to identify kinked flux rope dynamics with solar filament eruptions. Recent observations [2] have demonstrated that the MHD kink instability occurs in solar flux ropes which can disrupt yielding twisted magnetic clouds[3] that thread the solar system. The kink instability is important for MHD models of astrophysical jets [4, 5] and is often invoked to explain the observation of kinked structures in their synchrotron emission[6]. MHD kink modes are also observed in laboratory Z-pinch[7] and tokamak plasmas, and during spheromak formation are thought to mediate the conversion of toroidal to poloidal magnetic flux [8, 9]. In the applied field magneto-plasma thruster, the kink instability appears to deteriorate the performance of the thruster at high current[10, 11] and methods to suppress it are highly desirable[12].

The kink mode structure and stability condition are strongly dependent on the system geometry and the boundary conditions (BCs). Kruskal[13] and Shafranov [14] (hereafter referred to as KS) studied first the ideal MHD stability of a cylindrical plasma column with magnetic field components  $(0, B_\theta, B_z)$  using cylindrical coordinates  $(r, \theta, z)$ . They considered an infinitely long column and imposed helical perturbation of the form  $\xi = e^{i(\theta + 2\pi z/L)}$ , with  $\xi$  being the displacement of the plasma column from the equilibrium position. In order to account for the finite length of the system, a periodic boundary condition was used,  $k = 2\pi/L$ , where  $L$  is the system length. This yielded the following expression for the critical plasma current:

$$I_{KS} = (2\pi)^2 a^2 B_z / (\mu_0 L) \quad (1)$$

where  $a$  is the radius of the current channel.

The KS theory has been quite successful in predicting the behavior of toroidal plasmas for which the periodic BCs yield a proper accounting for the finite length of the system. In linear systems, however, substantial deviations from KS predictions can result from different axial BCs. The importance of the BCs has long been recognized[15, 16] and is of particular relevance to the stability of flux ropes line tied to the solar corona (*c.f.* Ref. [17] and survey Ref. [18]). In this case, the solar photosphere is assumed to be so much heavier to hold fixed the ends of flux ropes linked to it. The effect of line tying in linear systems have been subject of numerous theoretical (see Refs. [19–21] and references therein) and numerical investigations ([22] and references therein). In laboratory environments, the kink stability of a plasma column with line-tied ends has been experimentally investigated in linear devices, where line-tying is attributed to the presence of highly conducting end plates[23], and in open systems to a local discontinuity for the Alfvén velocity that forms a virtual boundary around the system[8, 10].

However, in Nature and laboratory line tying may not always describe satisfactorily the BC between the plasma and the surrounding environment. In the Solar corona, for example, flux ropes may become detached from the photosphere at one end. This situation may also arise in coronal holes where the field lines are open and one end extends into the solar system. Free-ended ropes may exist even in regions of normally closed field lines, during the dynamical evolution of the corona where reconnection can lead to the break up of field lines that get detached from the corona at one end thereby releasing energy from the corona outward into the solar system [24]. Similarly, in the case of jets from black holes, the tying of the rope is

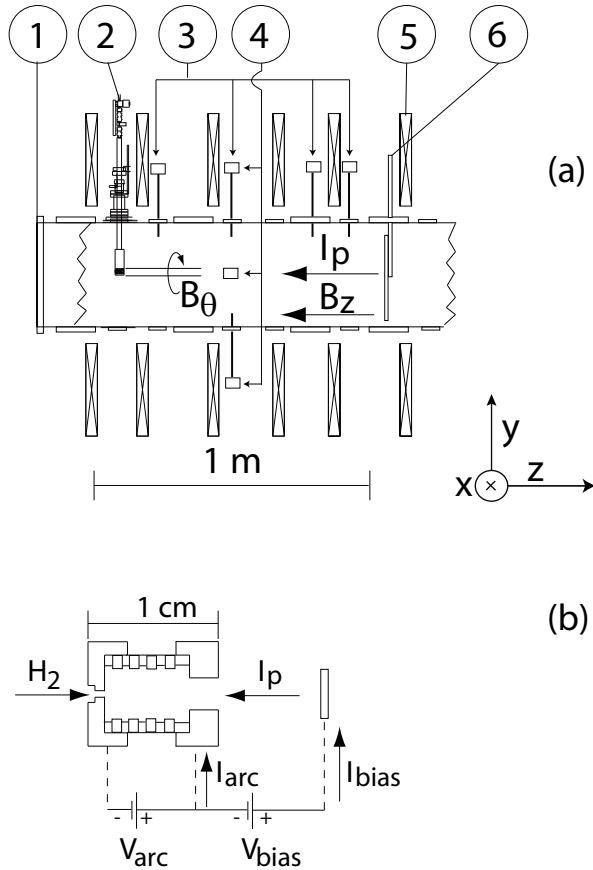


FIG. 1: (a) Experimental setup with diagnostics and coordinate system: (1) vacuum vessel; (2) plasma gun; magnetic probes in (3) an axial array and (4) an azimuthal array; (5) external coils; (6) external anode. (b) Expanded view of the miniaturized plasma injector with main circuit elements (not to scale).

working at one end only, at the end attached to the object creating the jet [25] (i.e. a black hole), but the other end of the jet can be free. In the laboratory, it has been shown that, in the presence of a sufficiently high plasma sheath resistance the plasma can be insulated from a perfectly conducting boundary leading to a free end flux rope[26].

In this article, we experimentally investigate the external kink instability in conditions where one end of the plasma column is line-tied to the plasma source, and the other end is not line-tied and therefore free to slide over the surface of the end-plate. The latter BC is a result of plasma sheath resistance that insulates, at least partially, the plasma from the end-plate. Compared to the line-tied case, we find significant differences in the kink mode structure and lower critical current for the onset of the kink. The experimental results agree with the predictions from a recent theory of the external kink instability for a slender plasma column[28].

The remainder of the article is organized as follows. In Section II, the experimental setup and the relevant diagnostics are described. The derivation of the kink the-

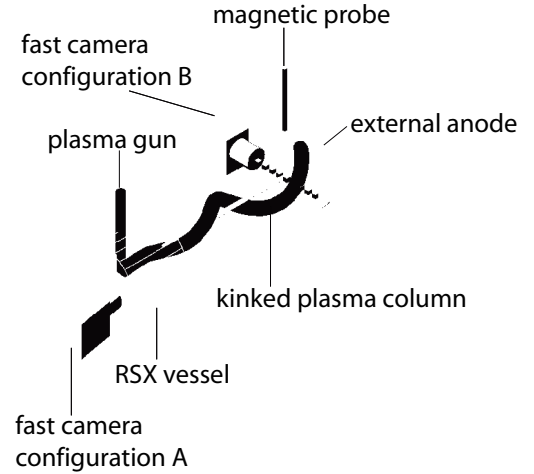


FIG. 2: Schematic three dimensional view of the fast CCD camera setup. Shown are the two possible camera views: (A) an end on view allows monitoring the global structure of the plasma column; (B) a lateral view in front of the external anode at the midplane images the plasma column along the  $x$  direction. Also schematically shown is the plasma column whose end rotates at the external anode.

ory in a non-line tied plasma column is briefly reviewed in Section III. Experimental data and comparison with theory are presented in Section IV. Finally, conclusions are summarized in Section V.

## II. EXPERIMENTAL SETUP AND DIAGNOSTICS

The experiments are conducted in the Reconnection Scaling Experiment (RSX) which uses electrostatic plasma guns to generate the plasma[29, 30]. Figure 1(a) shows the experimental setup with a view of the plasma gun located at  $z = 0$  and radially inserted into the center of the RSX cylindrical vacuum vessel (4 m length and radius  $b = 0.2$  m). The plasma gun contains a miniaturized plasma source with a circular  $0.79 \text{ cm}^2$  nozzle aperture, schematically represented in Fig. 1(b). A stack of molybdenum and boron nitride washers defines the arc channel between the anode and the cathode. A hydrogen gas is supplied through the cathode by an electromagnetic valve and a hydrogen plasma is produced by an arc discharge between the gun anode and the cathode. The arc plasma is maintained for  $< 10$  ms by a pulse forming network which is energized by a capacitor bank charged up to  $V_{arc} \approx 1$  kV. The arc current  $I_{arc}$  rapidly increases and reaches a maximum value of about 1 kA just before the external anode is biased. The pulse length is limited only by the gas inventory inside the gun volume and the pulse forming network. Detailed description of biasing circuits and control systems can be found in Ref. [29]. The hydrogen plasma is ejected from the gun and forms a cylindrical plasma column in a constant, uniform, axial

magnetic field of  $B_z = 120$  Gauss generated by external coils, Fig. 1-(5). Electron density and temperature have Gaussian profiles with half-maximum radius  $r_0 \approx 2$  cm such that  $r_0 \ll r_{wall}$ . Central electron density and temperature are  $n_{e0} = 1 - 3 \times 10^{19} \text{ cm}^{-3}$  and  $T_{e0} = 5 - 14$  eV, and axially decrease away from the gun. The axial velocity  $v_z \approx 5 - 7 \times 10^4$  m/s of the plasma has been estimated by solving the momentum balance equations for dominantly axial flow constrained by experimentally measured axial gradients in pressure and density.

A current is driven in the plasma by negatively biasing the gun anode with respect to an external anode as schematically shown in Fig. 1(b). The external anode is a  $50 \text{ cm}^2$  stainless steel plate which is electrically insulated from the vacuum vessel. A fraction  $I_{bias}$  of the arc current is diverted from the gun, where the electron current direction is towards the external anode. The bias discharge is initiated approximately 1 ms after the beginning of the arc discharge, corresponding to the maximum of  $I_{arc}$ . The applied bias voltage and the inductance of the total circuit including the plasma determine the slope of the applied current ramp typically  $dI_{bias}/dt < 10 - 20 \times 10^6 \text{ A/s}$ . The external anode can be positioned at different axial locations  $z = 0.3 - 3$  m allowing the length  $L$  of the current-carrying plasma column to be varied.

This experimental plasma has low enough temperature  $T_e < 20$  eV and short enough pulse length  $< 10$  ms to enable in situ measurements using internal probes together with external probes and optical systems. Internal probes, mainly magnetic and electrostatic arrays, are inserted into the vacuum vessel through flexible bellows and sliding seals, allowing two-dimensional scanning of plasma parameters in the  $x - y$  plane perpendicular to the axis of the device. Each probe can be moved along the axis of the device into a different porthole allowing measurements at various  $z$  locations. Fine spatial resolution in the  $x - y$  plane is achieved by moving internal probes between RSX discharges relying on highly reproducible plasma parameters[29]. The current density profile is computed from magnetic measurements in the  $x - y$  plane using miniaturized, two-dimensional magnetic probe arrays with ten pickup coils each with a total equivalent area turns of  $33 \times 10^{-4} \text{ m}^2$  equispaced by 2.5 mm. Two adjacent coils measure magnetic fields in orthogonal directions in space. Electron density  $n_e$ , temperature  $T_e$ , and pressure  $p_e = n_e T_e$  are simultaneously measured using a movable triple electrostatic probe with a 1 mm tip separation. Signals are digitized at 20 MHz providing adequate time resolution.

The MHD activity is monitored by two arrays of magnetic probes that include a total of seven coils inserted in the vacuum vessel at  $r = 15$  cm to measure the azimuthal magnetic field  $B_\theta$ . In the axial array, Fig. 1-(3), four magnetic probes are positioned at  $\theta = \pi/2$  (top of the vessel) and axially located at  $z = 0.14, 0.48, 0.62$  and  $0.76$  m. In the azimuthal array, Fig. 1-(4), the four magnetic probes are located at  $z = 48$  cm and azimuthally

equispaced by  $\pi/2$ . One magnetic probe is shared by the two arrays. Signals are passively integrated before digitizing at 20 MHz.

Images of the visible light (mostly  $H_\alpha$  at 656.3 nm) emitted by the plasma column are taken with a Cooke DiCam Pro intensified charge coupled device (ICCD) camera[31]. The CCD camera provides two 12-bit images, each with  $1280 \times 1024$  pixel resolution. Two geometrical arrangements are possible as schematically shown in Fig. 2: (A) the viewing perspective is end-on to the chamber allowing a global view of the column; (B) lateral view close to the external anode for precise measurements of column displacement over its surface. Calibration of pixels per centimeter is done using the known dimensions of the in situ probes. In the present set of experiments, Alfvén times are estimated to be somewhat long ( $> 1 \mu\text{s}$ ) as compared to the camera integration times (40 - 200 ns), so the images are likely to accurately resolve the plasma dynamics[32]. For our plasma conditions,  $H_\alpha$  emission, plasma density and current density profiles are approximately similar, such that the visible emission in Figs. 6(a,b) identify the position of the plasma column.

### III. KINK THEORY OF A NON-LINE TIED PLASMA COLUMN

The experimental results presented in this paper can be interpreted using a recently developed kink theory, first presented in Ref. [28], which includes axial plasma flow and one end of the plasma column that is free to move due to a non-line-tied boundary condition. The derivation of this model is briefly reviewed in this section.

We consider a plasma column with length  $L$  much exceeding its radius  $a$  and we use Cartesian coordinates with the axis  $z$  coinciding with the unperturbed axis of the column as shown in Fig. 1(a). For the  $m = 1$  kink mode, we consider perturbations which can be characterized by the "rigid" displacements of the "slices" of the plasma column in the  $x - y$  planes:  $\xi_x = \xi_x(z, t)$ ,  $\xi_y = \xi_y(z, t)$ ,  $\xi_z = 0$ . The deformation caused by the  $m = 1$  kink instability are such that the angle formed by the kinked column with its unperturbed direction remains small. This is a good approximation for a long-wavelength  $m = 1$  mode under condition  $a \ll b$ , where  $b$  is the radius of the conducting outer shell (i.e. the vacuum vessel). The axial magnetic field is large compared to the azimuthal magnetic field  $B_\theta/B_z \approx 2\pi a/L \ll 1$ . This corresponds to the standard scaling for the kink mode. The plasma pressure is assumed to be small compared to the magnetic pressure, so that the axial magnetic field is almost uniform.

By introducing a complex displacement [19, 20]

$$\zeta = \xi_x(z, t) + i\xi_y(z, t) \quad (2)$$

the MHD equation of motion for a plasma with an axial flow of speed  $v_z$ , constant along the  $z$  direction and

uniform in the  $x - y$  plane, is

$$\left(\frac{\partial}{\partial t} + v_z \frac{\partial}{\partial z}\right)^2 \zeta = v_A^2 \left(\frac{\partial^2 \zeta}{\partial z^2} + ik_0 \frac{\partial \zeta}{\partial z}\right) \quad (3)$$

where

$$k_0 = B_\theta / (aB_z) = \mu_0 I_p / (2\pi a^2 B_z) \quad (4)$$

and  $v_A \equiv \sqrt{2B_z / \sqrt{\mu_0 \rho}}$  where  $\rho = (2m_i / a^2) \int_0^a n_e(r) r dr$  ( $m_i$  is the ion mass, in our case hydrogen). For perturbations such as  $\exp(-i(\omega t - kz))$ , one finds

$$(\omega - kv_z)^2 = v_A^2 (k^2 + k_0 k) \quad (5)$$

or equivalently

$$k^2(1 - M^2) + k(k_0 + 2M \frac{\omega}{v_A}) - \frac{\omega^2}{v_A^2} = 0 \quad (6)$$

where  $M = v_z / (v_A)$  is the Alfvén Mach number.

By solving Eq. (6), we obtain that the eigensolution for the MHD equation of motion is

$$\zeta = (C_+ e^{ik_+ z} + C_- e^{ik_- z}) \quad (7)$$

with axial wave numbers

$$k_{\pm} = \frac{-2M \frac{\omega}{v_A} - k_0 \pm \sqrt{(2M \frac{\omega}{v_A} + k_0)^2 + 4 \frac{\omega^2}{v_A^2} (1 - M^2)}}{2(1 - M^2)}. \quad (8)$$

In the following, we limit ourselves to the analysis for the BCs that are relevant to the present set of experiments. Since the plasma column is line-tied at the plasma gun, we impose the condition of zero displacement at the surface  $z = 0$  and we obtain from Eq. (7) that  $C_+ = -C_- = C$ , and

$$\zeta = C(e^{ik_+ z} - e^{ik_- z}) \quad (9)$$

where  $C$  is an arbitrary normalization constant that we assume  $C = 1/2$ . In the case where the plasma is insulated from the external anode by a finite sheath resistance, the BC at  $z = L$  can be formulated as [28]

$$(\partial \zeta / \partial z + i(k_0/2)\zeta)|_{z=L} = 0. \quad (10)$$

Using a terminology already introduced in Ref. [26], we will refer to this condition as to *perfect non-line-tying* (PNLT) BC and, in Section IV B, we will show that it holds at the external anode for the present experiments, after using an equivalent condition that can be directly compared with experimental data.

Using Eq. (9), the PNL T BC provides the equation

$$\exp i(k_+ - k_-)L = \frac{2k_- + k_0}{2k_+ + k_0}. \quad (11)$$

which has to be solved with  $k_{\pm}$  given by Eq. (8). At the criticality, the right-hand-side in Eq. (11) is a real number since both the eigenfrequency  $\omega$  and the wavenumbers  $k_{\pm}$  are real, as can be verified from Eq. 8 in the

case  $M < 1$ . Therefore, the solutions of Eq. (11) must satisfy  $k_+ - k_- = (n\pi/L)$  where  $n$  is an integer number. Using this condition together with Eq. (8), we obtain the following equation

$$\omega^2 + \omega M k_0 v_A + \frac{v_A^2}{4} \left[ k_0^2 - \left(\frac{n\pi}{L}\right)^2 (1 - M^2)^2 \right] = 0 \quad (12)$$

which for  $n = 1$  provides the instability condition as follows

$$k_0 = \frac{\pi}{L} \sqrt{1 - M^2} \quad (13)$$

or equivalently in terms of the current

$$I_{crit} = \frac{1}{2} \frac{(2\pi a)^2 B_z}{\mu_0 L} (1 - M^2)^{1/2} \equiv \frac{I_{KS}}{2} \sqrt{1 - M^2}. \quad (14)$$

The equation above shows that the kink mode is unstable at half the KS current for vanishing flow and smaller currents when flow exists. This is due to the destabilizing effect of the centrifugal force related to the flow. We should note here that the presence of a line-tying BC at one end of the plasma column plays a paramount role in this. In an infinitely long system, the contribution of the flow can be eliminated by switching to the frame of reference where the fluid is at rest. In our case, however, this procedure does not work, as one end is line-tied to the resting wall. This makes it impossible to eliminate the flow by a coordinate transformation in a boundary-value problem.

The eigenfrequency  $\omega$  has a finite real component at the criticality

$$Re(\omega) = -\frac{\pi v_A}{2L} M \sqrt{1 - M^2} \quad (15)$$

which represents a rotation frequency of the perturbation since the mode under consideration is, azimuthally, the  $m = 1$  mode [Note a typo in the corresponding Eq. (71) of Ref. [28] and in Eq. (4) of Ref. [26], where the factor "2" in the denominator is missing]. For  $v_z$  directed from  $z = 0$  to  $z = L$ , the helix screws into the  $z = L$  electrode, independently of the direction of the  $z$  component of the magnetic field. Note that the frequency is nonzero at the stability margin. When we go beyond the stability margin, the rotation frequency increases.

Using Eq. (8) and Eq. (13), the axial wave numbers at the stability boundary are

$$k_{\pm} = \pm(\pi/2L) \left[ 1 \mp \sqrt{1 - M^2} \right]. \quad (16)$$

For the normalization  $C = 1/2$  that we use here and using Eq. (16), we find from Eq. (7),

$$\begin{aligned} \xi_x &= \frac{1}{2} (\cos \kappa_+ z - \cos \kappa_- z) \\ \xi_y &= \frac{1}{2} (\sin \kappa_+ z - \sin \kappa_- z) \end{aligned} \quad (17)$$

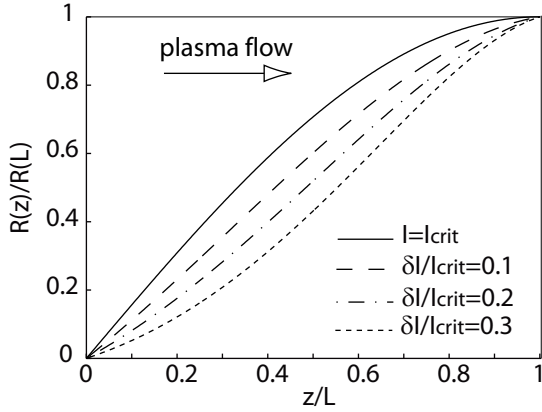


FIG. 3: Perturbed axis of the plasma column in the case of line tying at  $z = 0$  and perfect non-line tying at  $z = L$  according to Eq. 19. For slightly super-critical currents, the flow causes the advection of the perturbations resulting in a *skewing* of the eigenfunction in the direction of the plasma flow.

and therefore the perturbed axis of the plasma column form a helix which is wound over the axisymmetric surface with a radius

$$\frac{|R(z)|}{|R(L)|} = \sqrt{\xi_x^2 + \xi_y^2} = \sin\left(\frac{\pi z}{2L}\right) \quad (18)$$

which is represented as a continuous line in Fig. 3(a). From Eq. (18), we note that at the criticality the flow does not change the axial structure of the perturbed helix. The kink theory briefly reviewed here is a linear theory and therefore, strictly speaking, does not allow to resolve the plasma dynamics at the axial current substantially exceeding the threshold. However, the general structure of the perturbation determined by a linear eigenfunction should be quite a robust entity and thereby gives a hint on the shape of the column in the nonlinear regime. With this note of caution, beyond the stability margin for  $I > I_{crit}$ , the winding surface of the perturbed axis of the plasma column is different from Eq. (18):

$$\frac{|R(z)|}{|R(L)|} = \frac{\sqrt{1 - \cos[\pi \frac{z}{L}(1 + \frac{\delta I}{I_{crit}})]}}{\sqrt{1 - \cos[\pi(1 + \frac{\delta I}{I_{crit}})]}} e^{\frac{\pi^2}{2} \frac{\delta I}{I_{crit}} (\frac{z}{L} - 1)} \quad (19)$$

where  $\delta I = I - I_{crit}$ . The lengthy derivation of the equation above is presented in the Appendix. The drawback of this solution is in that, at small flow velocities, it has a very small applicability domain defined by the inequality:  $\delta I / I_{crit} \ll M^2$ .

In Fig. 3, we represent the perturbed axis of the plasma column according to Eq. (19) for different values of the plasma current. In the absence of flow in the super-critical regime, the eigenfunction does not change when increasing the plasma current according to Eq. 18. Conversely for slightly super-critical regimes, the presence of flow causes the advection of the perturbations re-

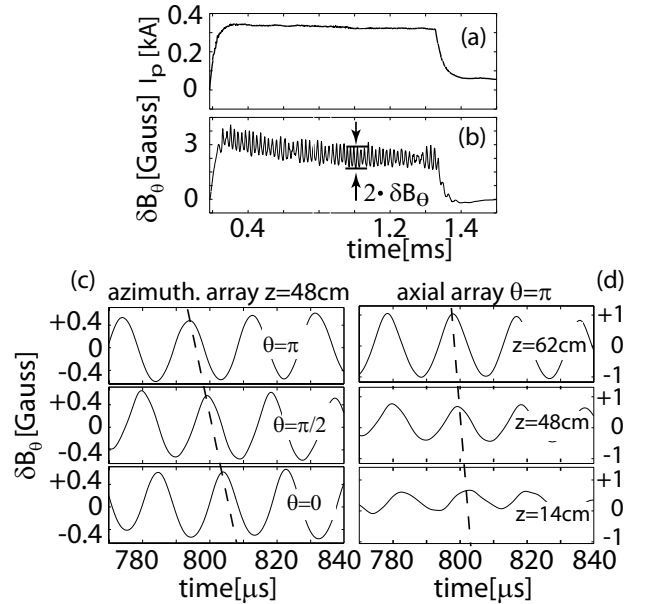


FIG. 4: Time histories of (a) the plasma current; (b) azimuthal magnetic field  $B_\theta$  at ( $z = 48$  cm,  $\theta = \pi/2$ ,  $r = 15$  cm). Expanded view of the temporal evolution of  $\delta B_\theta$  from azimuthal (c) and axial (d) arrays of magnetic probes during the stationary phase of the discharge.

sulting in a *skewing* of the eigenfunction in the direction of the plasma flow, which in this case is in the positive  $z$  direction.

#### IV. EXPERIMENTAL OBSERVATIONS OF KINK MODE

In this Section, we report on experimental observations of the kink mode in conditions where one end of the plasma column is line-tied to the plasma source, and the other end is not line-tied and therefore free to slide over the surface of the end-plate. We show that the latter BC is a result of plasma sheath resistance that insulates, at least partially, the plasma from the end-plate. The experimental results are compared with theoretical predictions derived in Sec. III.



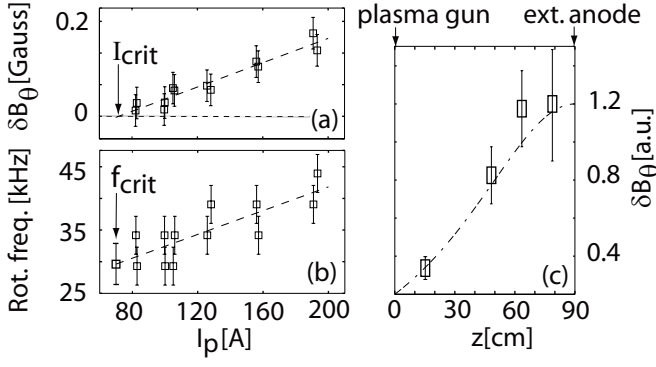


FIG. 5: (a) Amplitude of the perturbed azimuthal magnetic field,  $\delta B_\theta$ , and (b) rotation frequency of the mode during the stationary phase as a function of the plasma current  $I_p$ . (c) Axial structure of  $\delta B_\theta$  close to the instability threshold for  $I_p/I_{crit} \approx 1.2$  showing non-line-tied BC at the external anode. The dot-dashed line shows the structure of  $\delta B_\theta$  as predicted from theory.

### A. Kink mode structure and rotation

In Fig. 4(a), the time evolution of the plasma current measured at the external anode is shown for a discharge with  $L = 0.92$  m. The plasma current begins at  $t = 0$  when the bias is turned on (arc discharge starts at  $t = -1$  ms) and after  $\approx 150$   $\mu$ s reaches a stationary phase which lasts for  $\approx 1.4$  ms. The total plasma current  $I_p \approx 320$  A during the stationary phase is determined by the bias voltage and can be varied in the range  $I_p = 0.05 - 1$  kA. Figure 4(b) shows the time evolution of  $B_\theta$  as measured by the magnetic probe located at  $z = 48$  cm,  $\theta = \pi/2$ . For an expanded time window during the stationary phase, measurements of the perturbed azimuthal magnetic field  $\delta B_\theta$  from the azimuthal, Fig. 4(c), and the axial, Fig. 4(d), arrays of probes show oscillations with  $m = 1$  azimuthal periodicity at the frequency  $f \approx 50$  kHz. These oscillations are observed when the plasma current  $I_p$  exceeds a current threshold  $I_{crit}$  (see below), but are not detectable for  $I_p < I_{crit}$ . The observed instability growth time  $\tau_G \approx 4$   $\mu$ s is of the order of the axial Alfvén time. The  $m = 1$  azimuthal structure is consistent with a plasma column rotating as a rigid body at frequency  $f$ . The phase of the signals from the axial array increases linearly along the  $z$  direction, Fig. 4(d), indicating a rotating helical current channel. The kinked deformation is a right(left) handed helix if  $J_z \cdot B_z > 0$  ( $< 0$ ), as expected from a paramagnetic kink[8]. The direction of rotation reverses when reversing the external magnetic field  $B_z$ . In both cases, the mode rotation is such that the helix always *screws* into the external anode. This is consistent with prediction from Eq. 15 for a plasma flow directed from the gun to the external anode,

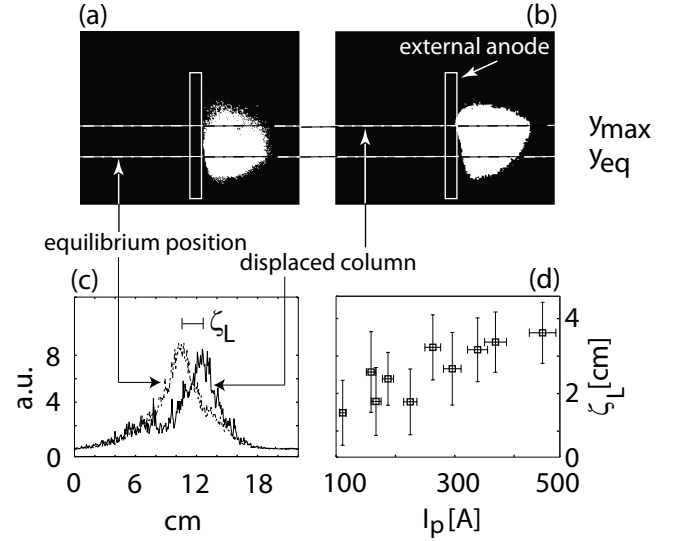


FIG. 6: Fast camera images of visible light emission from a lateral view near the external anode. As the plasma gun shoots from right to left, a fast gated image of visible emission shows (a) the equilibrium and (b) the displaced position of the plasma during the rotation. (c) Visible light emissivity profile along a line of sight parallel to the external anode and axially spaced 1 cm in front of it. The emissivity of the plasma column in the equilibrium position is artificially multiplied by a factor 2 for clarity. (d) Measured optical displacement  $\zeta_L = |y_{max} - y_{eq}|$  for different  $I_p$  values.  $y_{max}$  and  $y_{eq}$  are respectively the position of the maximum emissivity for the displaced column and for the column in the equilibrium position.

as in the present set of experiments.

For a series of discharges with plasma column length  $L = 0.92$  m and identical plasmas parameters, we varied the plasma current in the range  $86 \text{ A} < I_p < 190 \text{ A}$ . In Fig. 5(a,b), the rotation frequency and the average amplitude of the  $\delta B_\theta$  oscillations at the dominant frequency during the stationary phase are shown and scale linearly with  $I_p$ . This observation is in common to other linear plasma devices[10] and suggests that the predicted linear scaling from Eqs. (14), (15) may hold for slightly super-critical regimes.

In Fig. 5(a), the plasma current corresponding to the limit  $\delta B_\theta \rightarrow 0$  corresponds to the kink stability threshold which for these data is  $I_{crit} = 70 \pm 7$  A. The rotation frequency is also computed at the stability threshold which for the same data set is  $f_{crit} = 28 \pm 3.5$  kHz, Fig. 5(b).

In order to get insight into the axial structure of the mode close to criticality for  $I_p \approx 1.2 \times I_{crit}$ , Fig. 5(c) shows the amplitude of the perturbed magnetic field for the dominant  $m = 1$  mode from the axial array of magnetic probes. The most prominent feature of the axial structure is that while a line-tied BC holds at the gun, the large amplitude of the mode at  $z \geq 76$  cm can only occur if the plasma slides over the external anode and is therefore not line-tied. This is also confirmed by fast camera images of the plasma column at the external an-



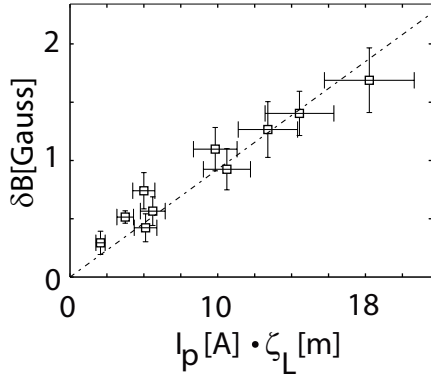


FIG. 7: Measurements at the external anode showing the perfect non line-tying condition of the plasma column. Magnetic field perturbations  $\delta B = (\delta B_x^2 + \delta B_y^2)^{1/2}$  are shown as a function of  $I_p \zeta_L$  and compared with predictions from Eq. (22) (dashed line).  $\zeta_L$  and  $\delta B_{x,y}$  are measured 1 cm in front of the external anode.

ode as shown in Fig. 6(a,b).

### B. Boundary condition at the external anode

The observed sliding of the plasma column over the external anode surface is not consistent with a line-tied BC, which might be presumed at the external anode for time scales less than its 100 – 200  $\mu$ s resistive diffusion time. Deviations from line-tying may appear if the plasma is insulated from the external anode by a finite plasma sheath resistance. The degree of insulation is measured by the ratio  $\kappa$  of the Alfvén transit to inductive decay times of the current[28] which can be estimated from the formula

$$\kappa \approx (c_s/v_z)[c/(a\omega_{pi})]^2 \beta_e^{1/2} \quad (20)$$

where  $c_s = (T_e/m_i)^{1/2}$ ,  $\beta_e = n_e T_e / B_z^2$  and  $\omega_{pi}$  is the plasma frequency (derivation in Ref. [28]). For typical RSX plasma parameters  $a \approx 2$  cm,  $T_e \approx 10$  eV,  $n_e \approx 10^{13}$  cm $^{-3}$ ,  $v_z/c_s \approx 1$ , we estimate  $\kappa \approx 15 \gg 1$ . This shows that the plasma is insulated from the conducting boundary by its finite sheath resistance and therefore a suitable BC at the external anode is given by Eq. 10. In the following, we derive a condition equivalent to the (PNLT) BC that can be directly compared with experimental data and we show that this holds at the external anode.

With a thin plasma column approximation ( $a \ll r_{wall}, L$ ) and assuming that  $r = 0$  is the equilibrium position, the Cartesian components of the perturbed magnetic field at  $r = r_p \gg a$  can be expressed as[34]

$$\delta B_{x,y} = (a^2/r_p^2) B_z (\pm \partial \xi_{x,y} / \partial z + k_0 \xi_{y,x}). \quad (21)$$

Using Eq. 10, in the vicinity of the external anode the perturbed magnetic field can be expressed as

$$\delta B = (\delta B_x^2 + \delta B_y^2)^{1/2} = I_p \zeta_L (3\mu_0) / (4\pi r_p^2) \quad (22)$$

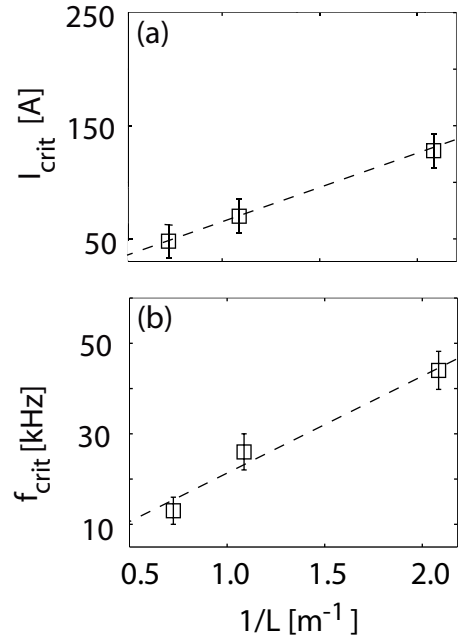


FIG. 8: For three different column lengths ( $L = 0.48, 0.92, 1.38$  m): (a) critical current  $I_{crit}$  (b) rotation frequency at the criticality  $f_{crit}$  as a function of the inverse column length  $1/L$ . The grey region indicates predictions from KS theory. Dotted lines show linear fits.

where  $\zeta_L = [\xi_x(L, t)^2 + \xi_y(L, t)^2]^{1/2}$ . This equation is equivalent to the PNLTC BC, given by Eq. 10, and can be directly compared with experimental data from magnetic probes and plasma column images near the external anode.

In Fig. 6, two fast-gated (200 ns gate  $\ll$  Alfvén time) images of visible light emission from the plasma near the external anode are shown before the onset of the kink instability, Fig. 6(a), and during the rotation at the time of maximum column displacement, Fig. 6(b), for a single discharge. The images are taken from a lateral view using the camera setup (A) as schematically shown in Fig. 2. Geometrical calibration of pixels per centimeter is done using the known dimensions of the in situ probes. The image in Fig. 6(b) is synchronized with a signal from a magnetic probe located at the same axial location but azimuthally separated by  $\pi/2$  to provide the position of maximum column displacement. We determine the visible light emissivity profile along a line of sight parallel to the external anode surface and axially spaced 1 cm in front of it. Fig. 6(c) shows profiles corresponding to Fig. 6(a-b). From these profiles, the maximum displacement  $\zeta_L = |y_{max} - y_{eq}|$  is computed where  $y_{max}$  and  $y_{eq}$  are respectively the position of the maximum emissivity for the displaced column and for the column in the equilibrium position. For a series of discharges that scan the plasma current in the range  $100 \text{ A} < I_p < 500 \text{ A}$ , Fig. 6(c) shows the almost linear relation between the experimental displacement  $\zeta_L = |y_{max} - y_{eq}|$  and the plasma current.

In Fig. 7, we compare the scaling predicted by Eq. 22 with the experimental data. The magnetic perturbations ( $\delta B_x, \delta B_y$ ) are measured at  $r_p = 17$  cm and 1 cm in front of the external anode using a bi-dimensional magnetic probe. The experimental data show excellent agreement with the PNLT predicted scaling in Eq. (22) (shown as a dashed line). We therefore conclude that PNLT BC apply to the external anode.

### C. Scaling of rotation and critical current with column length

To investigate the applicability of Eqs. (14), (15), we take advantage of the RSX experimental capability to adjust the length of the current carrying plasma column by moving the external anode along the  $z$  axis of the device. In a series of discharges, three different values of the column length are investigated  $L = 0.48, 0.92, 1.38$  m, while the other conditions are kept constant. Figure 8 shows (a) the critical current and (b) the rotation frequency at the criticality as a function of the inverse column length  $1/L$ . The deduced scalings  $I_{crit} = 59/L$  [A] and  $f_{crit} = 2.4 \times 10^4/L$  [Hz] is in agreement with a predicted linear scaling from Eqs. (14), (15).

The system comprising Eqs. (14), (15) provides a theoretical relationship between  $I_{crit}$ ,  $f_{crit}$ ,  $a$ ,  $M$  and the average plasma density (or Alfvén speed). This was solved using experimental measurements of the electron density profile at criticality (not shown here) together with deduced scalings  $I_{crit} = 59/L$  [A] and  $f_{crit} = 2.4 \times 10^4/L$  [Hz] from the data in Fig. 8. We obtained a radius  $a = 2 \pm 0.2$  cm which is in agreement with the experiment (see Fig. 9) and Mach number  $M = 0.25 - 0.4$ . The corresponding axial flow velocity  $v_z \approx 7 - 10 \times 10^4$  m/s is also consistent within the experimental uncertainties with the estimate in Sec. IV D. In Fig. 8, predictions from KS theory using the computed  $a$  are compared to the experimental data.

For the external kink, the plasma radius  $a$  is expected at the position where conductivity, magnetic diffusion time, and axial current density  $J_z(r)$  are negligibly small. This is experimentally tested using current density profile measurements at the criticality. Magnetic field profiles are measured using a miniaturized, two-dimensional magnetic probe which is inserted directly into the plasma column. For a plasma column length  $L = 0.92$  m, the radial profile of the azimuthal magnetic field  $B_\theta$  at  $z = 0.48$  m is assembled from magnetic probe measurements over a set of 40 discharges with same plasma parameters. The  $B_\theta$  profile at the criticality is shown in Fig. 9(a). The magnetic probe is radially scanned between two discharges providing a 5 mm spatial resolution.

Figure 9(b) shows a Bennet profile least-squares fit of the axial current density  $J_z(r)$  at the instability threshold, as obtained from data in Fig. 9(a). The previously determined radius  $a \approx 2 \pm 0.2$  cm is located at the edge of the profile where  $J_z(a) \approx 0.05 J_z(r=0)$  at the resolu-

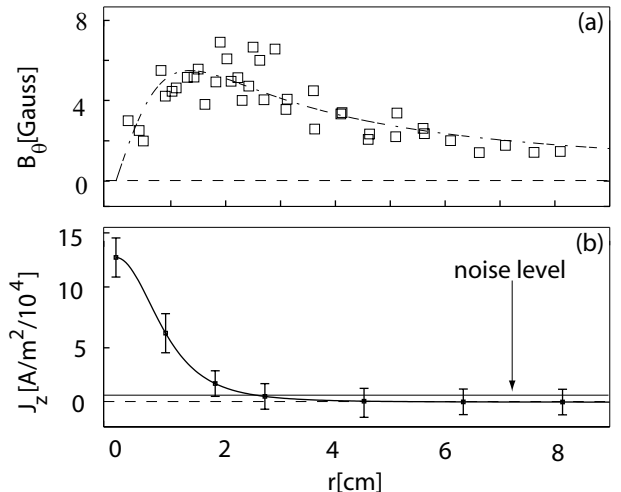


FIG. 9: Radial profiles at the criticality of (a) azimuthal magnetic field, (b) current density. Vertical grey region indicates the error bounded estimate of  $a$  at the edge of the current channel.

tion limit of the measurement. Similar conclusions follow from the magnetic diffusivity, derived from the measured electron temperature profile and the observed instability growth time  $\tau_G$ .

### D. Plasma flow

The plasma ejected from the gun is accelerated by the pressure gradient along the axis of plasma column. The downstream (far from the plasma gun) density and temperature in the plasma column are smaller than those near the gun (upstream ones), leading to the pressure gradient that provides the acceleration. The electric field does not exert any significant force on the plasma in the  $z$  direction. The electric force acting on the electrons is equal and opposite to the force acting on the ions under the quasi-neutrality condition, resulting in an axial current, but not in an axial flow.

For the unperturbed plasma column below criticality, the plasma flow velocity can be computed using the one-fluid MHD equation together with experimentally measured electron density and temperature profiles. Using a simple one-dimensional (1D) model in the one-fluid MHD approximation, the continuity equation and the equation of motion in the  $z$  direction can be respectively cast in the following discretized forms

$$\frac{d}{dt} \frac{(M_1 + M_2)}{2} + \frac{1}{\Delta z} (M_2 v_{z2} - M_1 v_{z1}) = 0 \quad (23)$$

$$\frac{d}{dt} \frac{(M_2 v_{z2} + M_1 v_{z1})}{2} + \frac{(M_2 v_{z2}^2 - M_1 v_{z1}^2)}{\Delta z} + \frac{(P_2 - P_1)}{\Delta z} = 0 \quad (24)$$

where  $M_j(t) = m_i \int n_e(r, z = z_j, t) 2\pi r dr$  is the linear mass,  $P_j(t) = \int n_e(r, z = z_j, t) T_e(r, z = z_j, t) 2\pi r dr$  is the

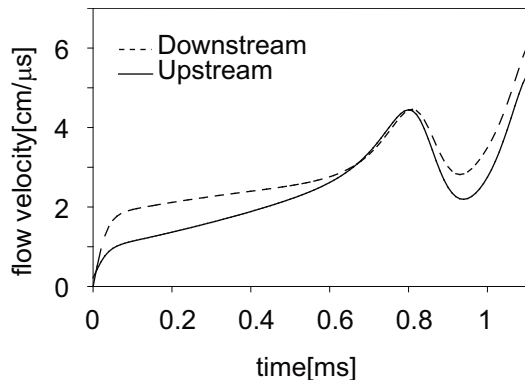


FIG. 10: Time evolution of the upstream and downstream plasma flow velocities as computed from the system of Eqs. 23,24. Time  $t = 0$  corresponds to the start of the plasma formation. The computation ends at  $t \approx 1.3$  ms corresponding to the critical current when the kink mode is destabilized.

gas dynamic linear force evaluated at  $z = z_j$ ,  $m_i$  is the ion mass, and  $v_{zj}$  is the axial flow speed at  $z = z_j$ .

Electron density  $n_e$ , temperature  $T_e$ , and pressure  $p_e = n_e T_e$  profiles are measured at two axial positions  $z_1 = 14$  cm and  $z_2 = 48$  cm over multiple discharges using a movable triple electrostatic probe with a 1 mm tip separation. The system of second-order differential equations given by Eqs. (23, 24) is numerically integrated using the experimental profiles providing the time evolution of the plasma flow velocity.

Fig. 10 shows the time evolution of the downstream and upstream flow velocities for the time interval  $t = 0 - \approx 1.3$  ms, where the time zero is referenced to the arc bias trigger when the plasma is formed. The end of the calculation approximately corresponds to criticality when the kink instability develops. It should also be noted that above the criticality, Eqs. (23, 24) cannot describe properly the flow in the helically perturbed column since the 1D assumption is not valid anymore. As can be seen from Fig. 10 the upstream and downstream velocities are very close to each other and reach a value  $v_z \approx 6$  cm/ $\mu$ s close to the criticality. This is consistent, within the experimental uncertainties, with the independent estimate provided in Sec. IV C. Future experiments are planned to measure plasma flow speed using a movable Mach probe which is presently under construction.

## V. CONCLUSIONS

During the past 50 years, much has been learned about the kink instability, but not much is known about the effect of axial boundary conditions. Most theoretical approaches have been either toroidal or axially periodic. We have argued that there are interesting natural and laboratory plasmas that are subject to non line tied axial boundary conditions and we have presented first experimental results for the current driven kink instability

in a plasma column with one free end that is not line-tied to its boundary. This rather peculiar boundary condition results from finite plasma sheath resistance that insulates, at least partially, the plasma from one end-plate. We have shown that mode structure and instability threshold are significantly different from predictions from the Kruskal-Shafranov theory and are accurately reproduced by a recently developed kink theory which we reviewed in Sec. III. The finite rotation of the mode, which is also observed in other laboratory devices[10, 23], is due to the plasma flow along the helically kinked plasma column.

Though not addressed here, the effect of a non-line-tied end should be important in the non-linear stage of the kink dynamics. For the relaxing kinked plasma column, a destabilizing  $J_\theta \times B_z$  force coexists with a stabilizing curvature force due to axial field line bending. The free end BC allows displacements with reduced curvature and restoring force which may result in a helical state saturated at larger level compared to the line-tied case. For the slightly super-critical case, this could be tested with a weakly non-linear theory such as the one suggested in Ref. [19], but with the effects of the plasma flow and sheath resistance included. The fully non-linear kink mode has been recently simulated [35] using the FLIP3D-MHD code which is based on the standard resistive MHD model[36]. Simulation results confirm present experimental findings and theoretical works[28] showing that free ended flux ropes are more susceptible to the kink instability.

## APPENDIX: EFFECT OF FLOW AT MODEST-TO-HIGH MACH NUMBERS NEAR THE STABILITY LIMIT

To solve the system of Eqs. (8), (11) in the case of small super-criticality, we introduce the following dimension-less variables (denoted by the wave):

$$\tilde{k}_0 = \frac{k_0 L}{\pi \sqrt{1 - M^2}} \quad (\text{A.1})$$

$$\tilde{\omega} = \frac{2L\omega}{\pi v_A M \sqrt{1 - M^2}} \quad (\text{A.2})$$

$$\tilde{k}_\pm = \frac{k_\pm L}{\pi} \quad (\text{A.3})$$

At the stability boundary,  $\tilde{k}_0 = 1$ ,  $\tilde{\omega} = -1$ .

Using the new dimensionless variables, Eqs. (8), (11) can be written as

$$\exp i\pi(\tilde{k}_+ - \tilde{k}_-) = \frac{2\tilde{k}_- + \tilde{k}_0 \sqrt{1 - M^2}}{2\tilde{k}_+ + \tilde{k}_0 \sqrt{1 - M^2}} \quad (\text{A.4})$$

$$k_{\pm} = \frac{-M^2\tilde{\omega} - \tilde{k}_0 \pm \sqrt{M^2\tilde{\omega}^2 + 2M^2\tilde{\omega}\tilde{k}_0 + \tilde{k}_0^2}}{2\sqrt{1-M^2}}. \quad (\text{A.5})$$

Near the stability boundary, a solution to the system of Eqs. (A.4), (A.5) can be found for  $\tilde{k}_0 = 1 + q$  and  $\tilde{\omega} = -1 + \epsilon$  where both  $q$  and  $\epsilon$  are small quantities. By expanding  $\tilde{k}_{\pm}$  in Eq. (A.5) up to the linear terms, we find

$$k_{\pm} \approx \frac{\pm 1 - \sqrt{1-M^2}}{2} - \frac{M^2}{2\sqrt{1-M^2}}\epsilon + \frac{\pm\sqrt{1-M^2}-1}{2\sqrt{1-M^2}}q \quad (\text{A.6})$$

and therefore

$$\exp(\tilde{k}_+ - \tilde{k}_-) \approx -1 - i\pi q, \quad (\text{A.7})$$

whereas

$$\frac{2\tilde{k}_- + \tilde{k}_0\sqrt{1-M^2}}{2\tilde{k}_+ + \tilde{k}_0\sqrt{1-M^2}} \approx -1 - \frac{2M^2}{\sqrt{1-M^2}}\epsilon - \frac{2M^2}{\sqrt{1-M^2}}q. \quad (\text{A.8})$$

By substituting Eqs. (A.8) and (A.9) into Eq. (A.4), one obtains a relationship between  $\epsilon$  and  $q$ :

$$\epsilon \approx -q + i\pi q \frac{\sqrt{1-M^2}}{2M^2} \quad (\text{A.9})$$

which yields the following expression for the wave numbers in Eq. (A.5)

$$\tilde{k}_{\pm} \approx \frac{\pm 1 - \sqrt{1-M^2}}{2} - i\frac{\pi q}{2} \pm \frac{q}{2}. \quad (\text{A.10})$$

The validity domain of the solution above is defined by the inequality  $q \ll M^2$ .

Noting that  $q = \frac{(k_0 - k_{0crit})L}{\pi\sqrt{1-M^2}}$  and returning to the initial notation, we find

$$\begin{aligned} \delta\omega &= \frac{\pi v_A M \sqrt{1-M^2}}{2L} \epsilon \\ &\approx \frac{M v_A (k_0 - k_{0crit})}{2} \left[ -1 + i\pi \frac{\sqrt{1-M^2}}{2M^2} \right] \end{aligned} \quad (\text{A.11})$$

$$k_{\pm} = \frac{\pi(\pm 1 - \sqrt{1-M^2})}{2L} + \frac{\pm i\pi + 1}{2} \frac{(k_0 - k_{0crit})}{\sqrt{1-M^2}}. \quad (\text{A.12})$$

Now, using the fact that  $k_+ - k_-$  is purely real, we have from Eq. (2) that the surface of revolution over which the column is wound is

$$\frac{|R(z)|}{|R(L)|} = \frac{\sqrt{1 - \cos(k_+ - k_-)z}}{\sqrt{1 - \cos(k_+ - k_-)L}} e^{(L-z)Im(k_-)}. \quad (\text{A.13})$$

We note that, for a given Mach number,  $k_0$  is a linear function of the plasma current and therefore

$$k_0 - k_{0crit} = k_{0crit} \frac{I - I_{crit}}{I_{crit}} = \frac{\pi\sqrt{1-M^2}}{L} \frac{\delta I}{I_{crit}} \quad (\text{A.14})$$

where  $\delta I = I - I_{crit}$ . Then from Eq. (A.12), we find:

$$k_{\pm} \approx \frac{\pi(\pm 1 - \sqrt{1-M^2})}{2L} + \frac{-i\pi \pm 1}{2L} \frac{\delta I}{I_{crit}} \quad (\text{A.15})$$

and

$$k_+ - k_- = \frac{\pi}{L} \left( 1 + \frac{\delta I}{I_{crit}} \right) \quad (\text{A.16})$$

$$Im(k_-) = -\frac{\pi^2}{2L} \frac{\delta I}{I_{crit}} \quad (\text{A.17})$$

so that Eq. (19) can easily be derived from Eq. (A.13).

## ACKNOWLEDGMENTS

The authors gratefully acknowledge useful discussions with F. Porcelli and J. M. Finn. This work was supported by Los Alamos National Laboratory, U.S. Department of Energy under Contract No. W-7405-ENG-36, and the Los Alamos Laboratory Directed Research and Development - Exploratory Research program.

Work supported in part under the auspices of the U. S. DOE by UC, LLNL under contract W-7405-Eng-48.

- [1] T. Sakurai, PASJ **28**, 177 (1976).
- [2] D. M. Rust, B. J. LaBonte, APJ **622**, L69 (2005).
- [3] A. Kumar, D. M. Rust, J. Geophys. Res. **101**, 15667 (1996).
- [4] R.V.E. Lovelace, Nature **262**, 649 (1976).
- [5] H. Li, G. Lapenta, J.M. Finn, S. Li and S.A. Colgate, Astrophysical Journal **643**, 92 (2006).
- [6] G. Benford, Mon. Not. R. Astron. Soc. **285**, 573 (1997).
- [7] A.J.L. Verhage, A. S. Furzer, D. C.. Robinson, Nucl. Fusion **18** 457 (1978).
- [8] S. C. Hsu and P. M. Bellan, Phys. Rev. Lett. **90**, 215002 (2003).
- [9] S. C. Hsu and P. M. Bellan, Phys. Plasmas **12**, 032103

- (2005).
- [10] M. Zuin *et al.*, Phys. Rev. Lett. **92**, 225003 (2004).
- [11] M. Zuin, *et al.*, Phys. Plasmas **11**, 4761 (2004).
- [12] M. Zuin, *et al.*, Appl. Phys. Lett. **89**, 041504 (2006).
- [13] M. Kruskal and J. Tuck, Proc. R. Soc. A **245**, 222 (1958).
- [14] V. D. Shafranov, At. Energ. **5**, 38 (1956).
- [15] L. S. Solov'ev, Sov. At. Energy **30**, 14 (1971).
- [16] M. A. Raadu, Sol. Phys. **22**, 425 (1972).
- [17] H. Baty, Astron. Astrophys. **318**, 621 (1997).
- [18] A. W. Hood, Plasma Phys. Contr. Fus. **34**, 411 (1992).
- [19] I. M. Lanskii and A. I. Shchetnikov, Sov. J. Plasma Phys. **16**, 322 (1990).
- [20] D. D. Ryutov, R. H. Cohen and L. D. Pearlstein, Phys.

- Plasmas **11**, 4740 (2004).
- [21] C. C. Hegna, Phys. Plasmas **11**, 4230 (2004).
  - [22] S. Inoue and K. Jusano, Astrophys. J. **645**, 742 (2006).
  - [23] W. F. Bergerson *et al.*, Phys. Rev. Lett. **96**, 015004 (2006).
  - [24] E. Priest and T. Forbes, Magnetic Reconnection: MHD Theory and Applications: Cambridge University Press, Cambridge **33**, 448 (2005).
  - [25] R. Blandford, Science **295**, 1653 (2002).
  - [26] I. Furno, T.P. Intrator, D.D. Ryutov, S. Abbate, T. Madziwa-Nussinov, A. Light, L. Dorf and G. Lapenta, Phys. Rev. Lett. **97**, 015002 (2006).
  - [27] D. L. Meier, S. Koide and Y. Uchida, Science **291**, 84 (2001).
  - [28] D. D. Ryutov, *et al.*, Phys. Plasmas **13**, 032105 (2006).
  - [29] I. Furno, *et al.*, Rev. Sci. Instrum. **4**, 141 (2003).
  - [30] I. Furno, *et al.*, Phys. Plasmas **12**, 055702 (2005).
  - [31] E. Hemsing, I. Furno, T. Intrator, and D. Wei, Rev. Sci. Instrum. **75**, 4106 (2005).
  - [32] E. Hemsing, I. Furno and T. Intrator, IEEE Trans. Plasma Sci. **33**, 448 (2005).
  - [33] E. G. Evstatiev, G. L. Delzanno and J. M. Finn, Phys. Plasmas **13**, 072902 (2006).
  - [34] J. D. Jackson, IEEE Trans. Plasma Sci. **33**, 448 (2005).
  - [35] G. Lapenta, I. Furno, T. P. Intrator, G. L. Delzanno, Accepted for publication in Journ. Geo. Research.
  - [36] J.U. Brackbill, J. Comp. Phys. **96**, 163 (1991).